



Crystal structure and X-ray absorption spectroscopy of trimethylarsine oxide dihydrate, (CH₃)₃AsO·2H₂O

Joel W. Reid ^{1,a)}, James A. Kaduk ², and Peter E. R. Blanchard¹

¹Canadian Light Source, 44 Innovation Boulevard, Saskatoon, SK S7N 2V3, Canada

²Illinois Institute of Technology, 3101 S. Dearborn St., Chicago, Illinois 60616, USA

(Received 29 April 2020; accepted 5 June 2020)

The crystal structure of trimethylarsine oxide dihydrate, (CH₃)₃AsO·2H₂O, (TMAO dihydrate) has been solved using parallel tempering with the FOX software package and refined using synchrotron powder diffraction data obtained from beamline 08B1-1 at the Canadian Light Source. Rietveld refinement, performed with the software package GSASII, yielded orthorhombic lattice parameters of $a = 13.3937(4)$ Å, $b = 9.53025(30)$ Å, and $c = 11.5951(3)$ Å ($Z = 8$, space group *Pbca*). The Rietveld refined structure was compared with density functional theory calculations performed with VASP and shows reasonable agreement. Arsenic K-edge X-ray absorption spectroscopy analysis also revealed additional information on the electronic structure of the arsenic atom within the TMAO dihydrate structure. © 2020 International Centre for Diffraction Data.

[doi:10.1017/S0885715620000421]

Key words: trimethylarsine oxide dihydrate, powder diffraction, structure solution, density functional theory, X-ray absorption spectroscopy

I. INTRODUCTION

Arsenic (As) is a ubiquitous element in the environment (Cullen and Reimer, 1989; Matschullat, 2011) with numerous anthropogenic sources (Chen *et al.*, 2016) and significant toxicity to biota (Capitani, 2011). These criteria have generally led arsenic to be considered among the most impactful environmental toxins (ATSDR, 2020).

Trimethylarsine oxide, TMAO (IUPAC name dimethylarsorylmethane, chemical formula (CH₃)₃AsO), is one of a number of biochemically important methylated organic arsenic species (Cullen *et al.*, 2016). It is an important compound in arsenic biomethylation and metabolism because it can be quickly reduced by some biological species to trimethylarsine, (CH₃)₃As, which is both volatile and mobile (Pickett *et al.*, 1988). TMAO has been observed as the dominant organic arsenic species identified during monsoonal wet deposition in areas of the Indian subcontinent, including Bangladesh and Sri Lanka (Savage *et al.*, 2017). Arsenic tends to be more prevalent in marine organisms than terrestrial ones. While arsenobetaine, (CH₃)₃AsCH₂CO₂, is typically the predominant arsenic compound found in marine organisms, TMAO has been observed as a minor arsenic component in a number of fish species (Cullen and Reimer, 1989; Hunter *et al.*, 1998).

This paper presents the crystal structure of TMAO dihydrate, provides a complete Bragg reflection list for phase identification, and discusses some additional insights regarding the electronic and local structure of the arsenic atom provided by complementary X-ray absorption spectroscopy (X-ray

absorption near-edge structure (XANES) and extended X-ray absorption fine-structure (EXAFS)).

II. EXPERIMENTAL

A specimen of TMAO prepared by Toronto Research Chemicals was lightly ground with a mortar and pestle. The specimen was mounted in a 0.3 mm ID polyimide capillary and taken immediately for data collection because of the hygroscopic nature of the compound.

Powder X-ray diffraction (PXRD) patterns were collected using a Canadian Macromolecular Crystallography Facility beamline (08B1-1; Fodje *et al.*, 2014) at the Canadian Light Source (CLS). 08B1-1 is a bending magnet beamline with a Si (111) double crystal monochromator. Two-dimensional (2D) data were obtained using a Rayonix MX300HE detector with an active area of 300 × 300 mm². The patterns were collected at an energy of 18 keV ($\lambda = 0.68918$ Å) and a sample-detector distance of 150 mm.

The 2D PXRD patterns were calibrated and integrated using the GSASII software package (Toby and Von Dreele, 2013). The sample-detector distance, detector centering, tilt, and wavelength were calibrated using a series of patterns obtained using a lanthanum hexaboride (LaB₆) standard reference material (NIST SRM 660a LaB₆), and the calibration parameters were applied to all patterns. After calibration, the 2D patterns were integrated to obtain standard powder diffraction patterns.

Ab initio indexing with DICVOL06 (Boultif and Louer, 2004) suggested an orthorhombic unit cell with lattice parameters $a = 13.3790$ Å, $b = 11.6060$ Å, $c = 9.5183$ Å and a cell volume of 1477.97 Å³ ($M_{20} = 18.2$, $F_{20} = 87.4$). Space group determination with ChekCell (Laugier and Bochu, 2000)

^{a)} Author to whom correspondence should be addressed. Electronic mail: joel.reid@lightsource.ca



suggested space group *Pbca* as the best solution, with the *b* and *c* axes switched from the original cell.

A TMAO molecule was extracted from the Cambridge Structural Database (CSD) entry ASOXCA (Ng *et al.*, 1977). The molecule was converted to a Fenske–Hall Z-matrix using Open Babel (O’Boyle *et al.*, 2011) for structure solution using parallel tempering with the FOX software package (Favre-Nicolin and Černý, 2002). Roughly 10 sets of parallel tempering with 2×10^6 trials/set resulted in multiple comparable solutions with cost functions of ~ 3000 .

Rietveld refinements of the crystal structure were performed with the GSASII program (Toby and Von Dreele, 2013) using a Thompson–Cox–Hastings modified pseudo-Voigt peak shape function (Thompson *et al.*, 1987). The background was modeled using a 20-term log interpolation function. Positional parameters were refined with soft restraints on bond distances and angles for the As, C, and O atoms in the TMAO molecule obtained using Mogul 1.8.3 (Bruno *et al.*, 2004). Hydrogen positions were left fixed during refinement but were periodically optimized using Avogadro (Hanwell *et al.*, 2012). The isotropic displacement parameters of the hydrogen atoms were constrained to be 1.3 times the value of the closest “heavy” atom.

The crystal data, data collection, and refinement details are summarized in Table I.

Density functional geometry optimization (using the fixed experimental unit cell) was begun using CRYSTAL14 (Dovesi *et al.*, 2014). The basis sets were obtained from the literature for the C, H, O (Gatti *et al.*, 1994), and As atoms (Peintinger *et al.*, 2013). The calculations were run on eight 2.1 GHz Xeon cores (each with 6 GB RAM) of a 304-core Dell Linux cluster at the Illinois Institute of Technology (IIT), used eight *k*-points and the B3LYP functional. The geometry optimization was completed using VASP (Kresse and Furthmüller, 1996) through the MedeA interface (Materials Design, 2016). The calculation was carried out on

sixteen 2.4 GHz processors (each with 4 GB RAM) of a 64-processor HP Proliant DL580 Generation 7 Linux cluster at North Central College. The calculation used the generalized gradient approximation (GGA)–Perdew–Burke–Ernzerhof (PBE) functional, a plane wave cutoff energy of 400.0 eV, and a *k*-point spacing of 0.5 \AA^{-1} leading to a $1 \times 2 \times 2$ mesh. A single-point calculation was carried out on the VASP-optimized structure using CRYSTAL14.

Arsenic (As) K-edge XANES spectra of TMAO and various arsenic standards were collected on the Hard X-ray MicroAnalysis (HXMA) beamline (06ID-1; Jiang *et al.*, 2007). 06ID-1 is a wiggler beamline equipped with a silicon (111) double crystal monochromator that provides a monochromatic flux of $\sim 6 \times 10^{11}$ photons/s, with a resolution of 1 eV at 10 keV. Spectra were recorded in transmission mode using ionization chambers filled with 100% helium and an X-ray beam size of 1×3 mm. Samples were cooled to ~ 77 K using a closed-cycle nitrogen cryostat to minimize X-ray beam-induced reduction during data collection. A gold foil standard was placed behind the sample and measured concurrently in transmission mode. The As K-edge spectra were calibrated against the gold foil with the maximum of the first derivative of the gold L_{3} -edge spectrum set to 11 919 eV with a step size of 0.3 eV near the edge jump (Ravel and Newville, 2005). The EXAFS spectrum of TMAO was collected up to 16k with a step size of 0.05k.

All XANES and EXAFS spectra were analyzed with the Athena and Artemis programs, respectively, included in the Demeter software package (Ravel and Newville, 2005). The EXAFS spectrum was analyzed by fitting the parameters of the standard EXAFS equation using the FEFF6 code (Rehy and Albers, 1990; Newville, 2004). The scattering cluster for the FEFF calculation was generated from the structure model obtained from the PXRD analysis. The amplitude reduction factor (S_0) and ΔE_0 were fitted as global parameters across all scattering paths. Individual Debye–Waller (σ^2) and ΔR factors were fitted for each single-scattering path. The goodness of the fit was monitored using the R_{fit} factor.

TABLE I. The crystal data, data collection, and refinement parameters obtained for TMAO dihydrate.

Crystal data	
Formula, <i>Z</i>	(CH ₃) ₃ AsO·2H ₂ O, <i>Z</i> = 8
Molecular mass (<i>M_r</i>)	172.06 g mol ^{−1}
Symmetry, space group	Orthorhombic, <i>Pbca</i> (61)
Unit cell parameters	<i>a</i> = 13.3937(4) Å, <i>b</i> = 9.53025(30) Å, and <i>c</i> = 11.5951(3) Å
Volume	1480.06(5) Å ³
Density (ρ_{calc})	1.544 g cm ^{−3}
Data collection	
Beamline	CLS 08B1-1
Monochromator	Si (111) double crystal monochromator
Detector	Rayonix MX300HE (300 × 300 mm ²)
Specimen mounting	0.3 mm Kapton capillary
Collection mode	Transmission
Wavelength	$\lambda = 0.68918 \text{ \AA}$
Collection range, step size	2–52° (2 θ), 0.01°/step (refinement region: 4–44°)
Refinement	
Number of data points	4001
Background correction	20-term log interpolation function
Number of refined parameters	49
<i>R_p</i>	0.00376
<i>R_{wp}</i>	0.00581
Reduced χ^2	1.06

III. RESULTS AND DISCUSSION

During data collection, it was noticed that the TMAO material was quite hygroscopic. With no grinding, the material produced noticeably grainy 2D powder patterns, but more than minimal grinding converted the material to a gel. Even with minimal grinding, by the end of data collection, the material in the capillary has an intermediate consistency between solid and liquid. Therefore, during structure solution, different levels of hydration were tested with FOX. Two water molecules per TMAO molecule provided the optimal model; the addition of a third water molecule always resulted in overlap and occupancy adjustment between two oxygen atoms during parallel tempering. The density functional theory (DFT) modeling provided confirmation that the (CH₃)₃AsO·2H₂O model (TMAO dihydrate) was reasonable.

The final Rietveld refinement for TMAO dihydrate is shown in Figure 1, showing the native refinement with background (top) and the background subtracted data with the pattern magnified by a factor of 3 above 15°, 2 θ (bottom). The significant background is likely related to both the hygroscopic nature of the compound and the fact that the data

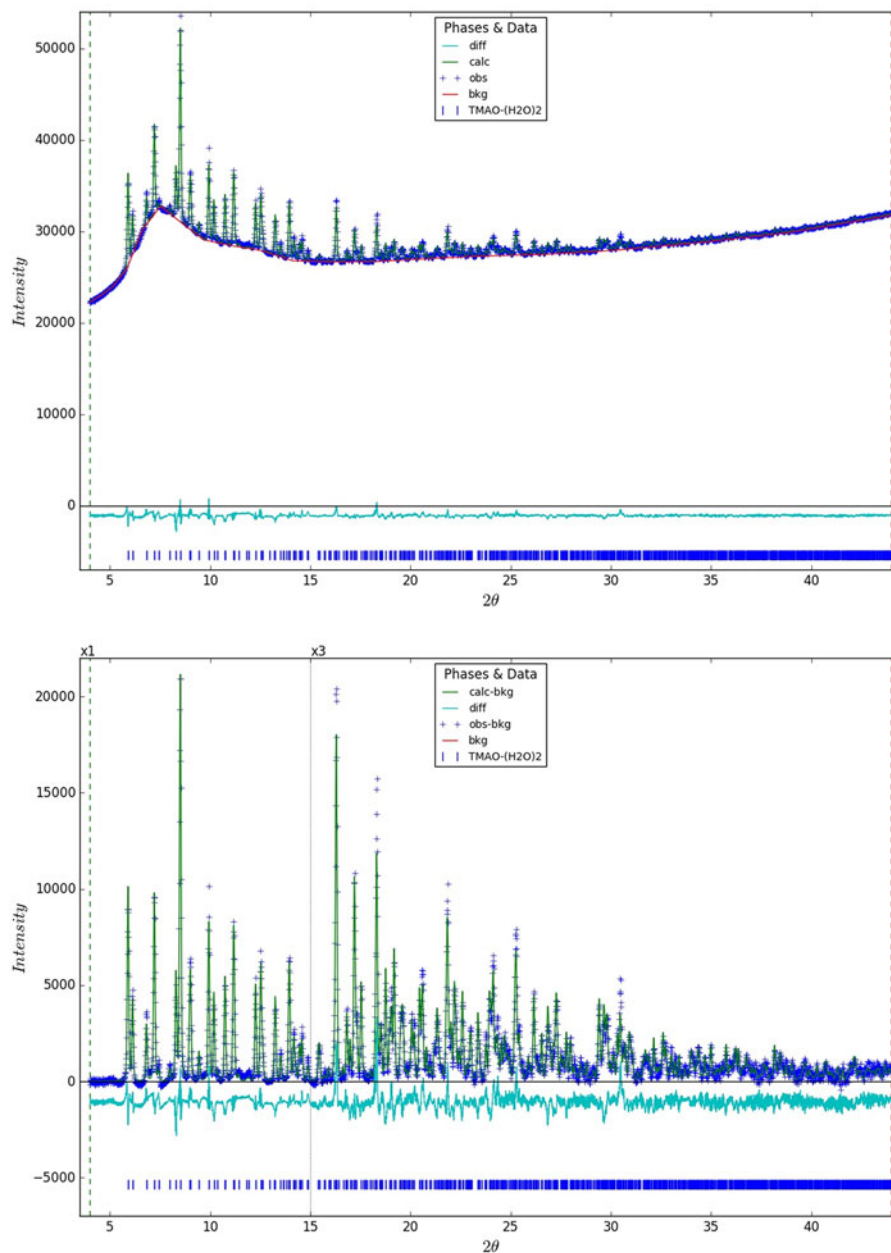


Figure 1. A plot illustrating the final Rietveld refinement of TMAO dihydrate obtained with GSASII (top). The data are presented background subtracted and magnified by a factor of 3 for the region above 15° , 2θ (bottom).

were collected ~ 6 keV above the absorption edge of arsenic (As K-edge: 11 867 eV).

The Rietveld refined atomic coordinates obtained with GSASII for TMAO dihydrate are given in Table II, while DFT optimized atomic coordinates obtained with VASP are given in Table III. The atomic labels given in the tables are illustrated in Figure 2. The difference between the Rietveld and DFT models was compared in two different ways. The root-mean square (RMS) Cartesian displacement, calculated using the definition of Van de Sreek and Neumann (2014), between the Rietveld refined atomic coordinates and the DFT model is 0.395 \AA . This value occupies the upper end of the “gray area” for agreement between correct powder structures and DFT models. Given some residual graininess of the powder because of minimal grinding, plus the large background and hygroscopic nature of the compound, the

discrepancy is probably not surprising. The RMS difference was also calculated using the molecular overlay function in Mercury (Macrae *et al.*, 2008) for the TMAO molecule and shows excellent agreement of 0.044 \AA . Mercury performs a least-squares alignment of the two molecules, resulting in the improved agreement compared with the absolute Cartesian displacement.

The DFT optimized model for TMAO dihydrate is illustrated in Figure 3 from an oblique view and along all three axes. The compound forms alternating layers of TMAO molecules and water molecules (two layers each per unit cell) parallel the *ab*-plane, with hydrogen bonding observed both within and between layers. The hydrogen bonds observed in the DFT optimized structure are summarized in Table IV. The hydrogen bond energies were calculated from the overlap populations using the correlation function of Rammohan and

TABLE II. The Rietveld refined crystal structure of TMAO dihydrate with lattice parameters $a = 13.3937(4)$ Å, $b = 9.53025(30)$ Å, and $c = 11.5951(3)$ Å. All atoms were refined with fixed site occupancies of 1.

Atom	x/a	y/b	z/c	Wyckoff	U_{iso} (Å ²)
As1	0.06367(16)	0.29302(21)	0.56790(16)	8c	0.0204(7)
O2	0.0103(7)	0.4034(9)	0.6625(9)	8c	0.042(4)
C3	0.1168(9)	0.1270(8)	0.6363(11)	8c	0.042(4)
C4	0.1683(8)	0.3933(11)	0.4911(10)	8c	0.042(4)
C5	-0.0339(7)	0.2331(11)	0.4571(8)	8c	0.042(4)
O6	0.8460(7)	1.0093(11)	0.6788(10)	8c	0.022(3)
O7	0.6821(7)	0.6885(14)	0.2119(9)	8c	0.022(3)
H8	0.1719	0.1550	0.6991	8c	0.055
H9	0.1504	0.0633	0.5710	8c	0.055
H10	0.0580	0.0696	0.6772	8c	0.055
H11	0.2226	0.4266	0.5530	8c	0.055
H12	0.1377	0.4831	0.4485	8c	0.055
H13	0.2031	0.3262	0.4289	8c	0.055
H14	-0.0937	0.1806	0.5006	8c	0.055
H15	0.0001	0.1628	0.3969	8c	0.055
H16	-0.0626	0.3225	0.4121	8c	0.055
H17	0.8994	0.9840	0.7273	8c	0.028
H18	0.7913	0.9576	0.6779	8c	0.028
H19	0.6798	0.7925	0.2162	8c	0.028
H20	0.6111	0.6584	0.2021	8c	0.028

Kaduk (2018). Each of the water molecules acts as a donor to the double-bonded O2 and as a donor to the other water molecule. The result is a 2D layer of hydrogen bonds parallel to the ab -plane. Several C–H...O hydrogen bonds are also present. Although individually weak, they contribute significantly to the crystal energy.

A Bragg reflection list was prepared by summing reflections closer than $0.03^\circ 2\theta$ as multiple reflections and assigning a weighted average reflection position, then including all reflections with relative integrated intensities of 0.5% or greater up to $30^\circ 2\theta$. The Bragg reflection list and raw data are contained in a crystallographic information file (CIF) in the online supplementary material, along with individual CIF files for the Rietveld refined and DFT optimized structures.

TABLE III. The DFT optimized crystal structure of TMAO dihydrate with fixed lattice parameters $a = 13.39364$ Å, $b = 9.53007$ Å, and $c = 11.59516$ Å.

Atom	x/a	y/b	z/c
As1	0.06701	0.28726	0.56108
O2	0.01660	0.38328	0.67137
C3	0.09282	0.09580	0.60800
C4	0.19289	0.36698	0.51335
C5	-0.02186	0.28425	0.43012
O6	0.83481	0.99078	0.70067
O7	0.68102	0.69337	0.20463
H8	0.15068	0.09590	0.67487
H9	0.11878	0.03854	0.53147
H10	0.02358	0.05016	0.64141
H11	0.24068	0.37451	0.58996
H12	0.17926	0.47114	0.47642
H13	0.22719	0.29802	0.44861
H14	-0.09496	0.24623	0.45872
H15	0.00869	0.21469	0.36331
H16	-0.02720	0.39188	0.39651
H17	0.88821	0.96552	0.74914
H18	0.78010	0.93907	0.69983
H19	0.67869	0.79736	0.20895
H20	0.61000	0.66328	0.19491

Arsenic K-edge XANES analysis provided information on the local electronic structure of arsenic atoms in TMAO dihydrate. The As K-edge XANES spectrum of TMAO dihydrate was compared with other organic and inorganic arsenic species as shown in Figure 4. Although the As K-edge XANES spectrum of TMAO has been used for analyzing the presence of organic arsenic species in biological and environmental samples (Smith *et al.*, 2005; Koch *et al.*, 2007; George *et al.*, 2009; Foust *et al.*, 2016), spectral features have not been well discussed. The major feature in the As K-edge is the white line feature at corresponding to the dipole-allowed transition of an As 1s electron into unoccupied As 4p states. The absorption energy of this feature is generally sensitive to changes in bonding character, particularly oxidation state and covalency (Bunker, 2010). This is best illustrated when comparing inorganic arsenic species of different oxidation states [Figure 4(a)]. In general, the As K-edge absorption energy increases with increasing oxidation state, as core electrons are more tightly bound to the nucleus of

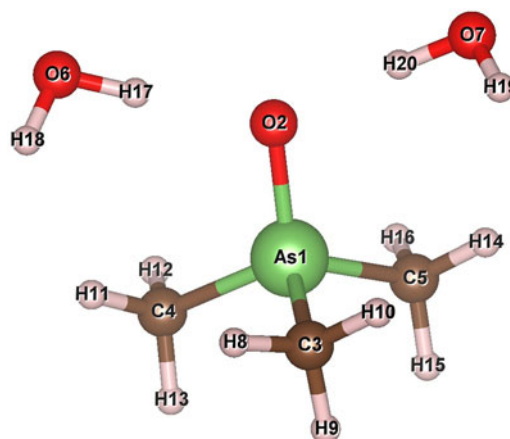


Figure 2. The atom labels used for the description of the TMAO and water molecules. The figure was prepared with VESTA (Momma and Izumi, 2011).

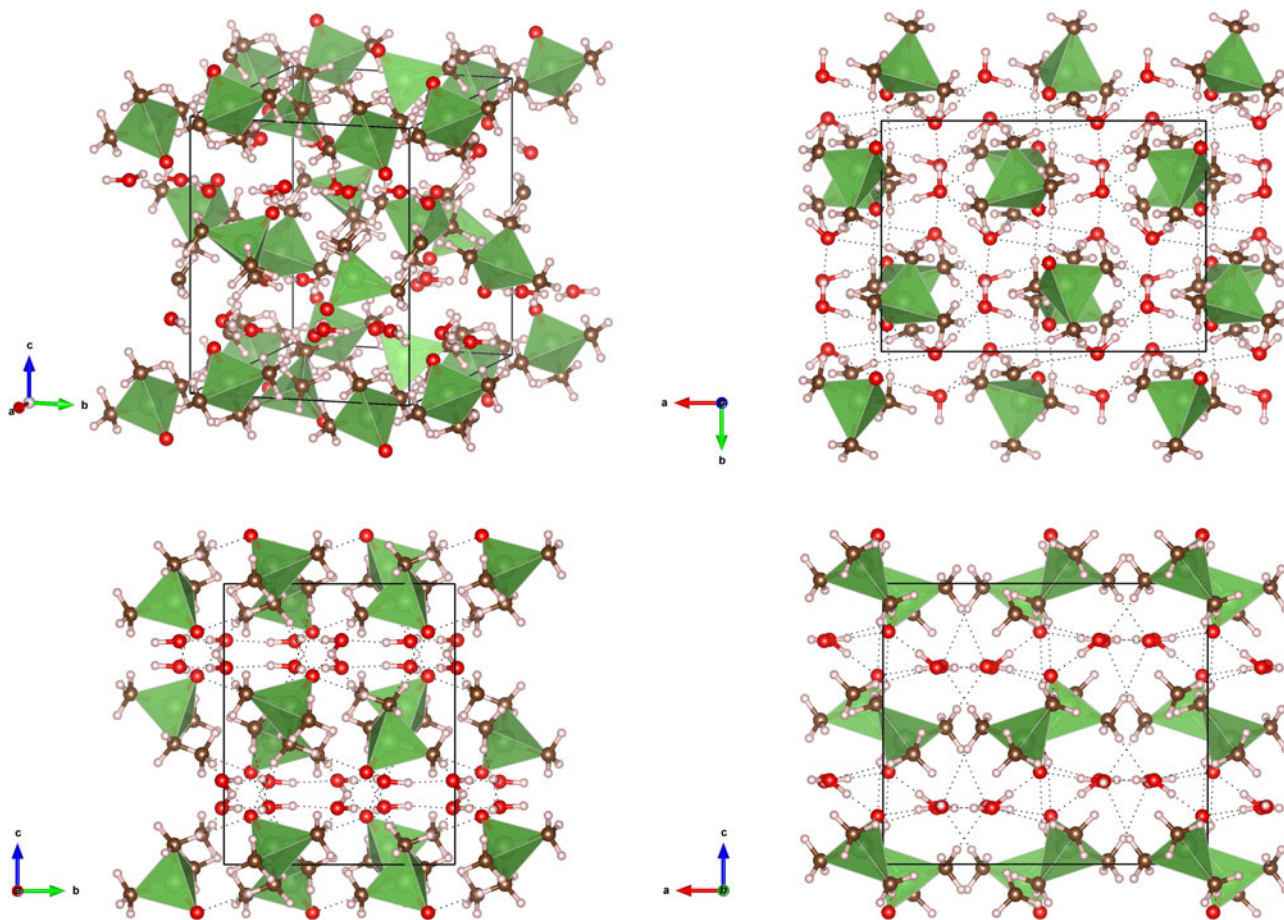


Figure 3. The DFT optimized crystal structure of TMAO dihydrate from an oblique view (top left), and viewed along the *c*-axis (top right), *b*-axis (bottom right), and *a*-axis (bottom left). The atom types can be identified by color, including arsenic (green tetrahedra), carbon (brown), oxygen (red), and hydrogen (pink). Hydrogen bonds are illustrated by the dotted black lines in the on-axis views. The unit cell is outlined in black. The figure was prepared with VESTA (Momma and Izumi, 2011).

that atom because of the greater positive charge. As such, more energy is required to remove the core electron (Smith *et al.*, 2005). The absorption energy of TMAO dihydrate is significantly less than that of inorganic arsenate species, indicating that As–O bonds are more covalent in TMAO compared with inorganic arsenate species. Surprisingly, the absorption energy of TMAO is nearly identical to that of monomethylarsonic acid (MMA) and dimethylarsinic acid (DMA), suggesting that the effective oxidation state of arsenic is mostly influenced by the As–O bonds rather than the As–OH and As–CH₃ bonds. However, replacing methyl groups with hydroxyl groups does seem to result in a broadening of

the As K-edge white line, possibly suggesting that As 4p states become more delocalized.

The fitted Fourier-transformed As K-edge EXAFS spectrum of TMAO dihydrate is shown in Figure 5. A summary of the EXAFS fitting results is shown in Table V. The first shell As1–O2 and As1–C, and third shell As1–O6 and As1–O7 scattering paths were included in the fitting model. Attempts were made to include second shell As–H scattering paths. However, these and several multiple-scattering paths were found to have negligible influence on R_{fit} and were ultimately excluded from the final fit of the EXAFS spectrum.

TABLE IV. Hydrogen bonds observed in the TMAO dihydrate structure and their parameters as determined by the DFT modeling.

H-Bond	D–H (Å)	H...A (Å)	D...A (Å)	D–H...A (°)	Overlap (<i>e</i>)	E (kcal mol ^{−1})
O7–H20...O2	1.000	1.774	2.773	176.8	0.061	13.5
O7–H19...O6	0.993	1.855	2.843	173.0	0.057	13.0
O6–H18...O7	0.992	1.832	2.824	177.4	0.049	12.1
O6–H17...O2	1.000	1.758	2.757	177.2	0.055	12.8
C5–H16...O2	1.100	2.287	3.381	172.7	0.031	
C5–H15...O2	1.099	2.416	3.437	154.0	0.021	
C4–H13...O7	1.098	2.380	3.461	167.7	0.031	
C4–H11...O7	1.097	2.682	3.725	158.7	0.017	
C3–H10...O6	1.095	2.649	3.712	163.4	0.012	

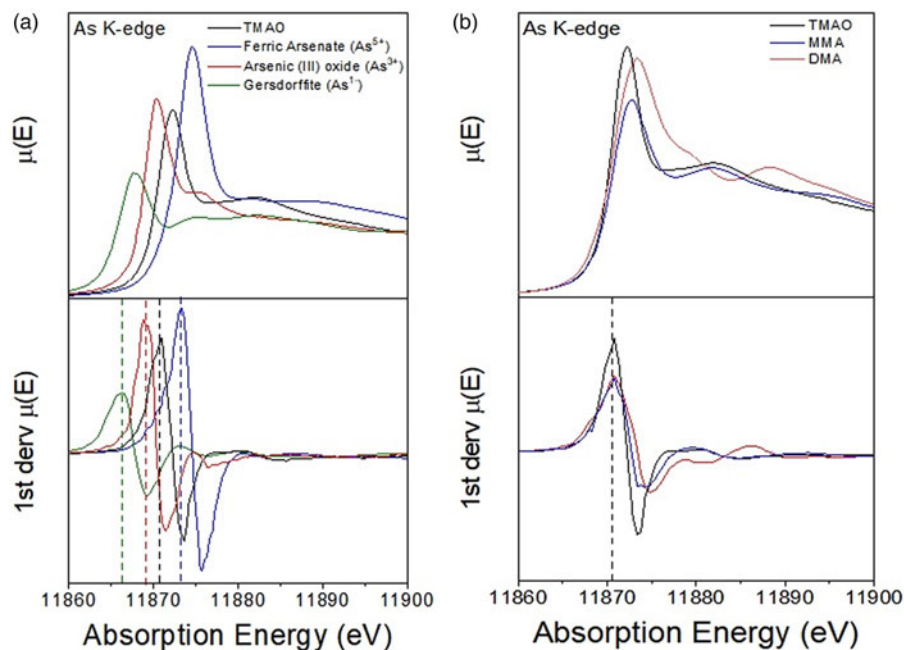


Figure 4. (a) The As K-edge XANES spectrum of TMAO dihydrate compared with ferric arsenate (As^{5+}), arsenic (III) oxide (As^{3+}), and gersdorffite (As^{1-}). Normalized transmission spectra are shown on the top, and the first derivative spectra are shown on the bottom. Dashed lines corresponds to the As K-edge absorption energies of TMAO dihydrate (black line; 11 870.9 eV), ferric arsenate (blue line; 11 873.3 eV), arsenic (III) oxide (red line; 11 869.1 eV), and gersdorffite (green line; 11 866.3 eV). As–O bond in TMAO is generally more covalent than in arsenate species. (b) The As K-edge XANES spectra of TMAO dihydrate compared with MMA and DMA. All three organic arsenic species have nearly identical absorption energies (11 870.9 eV).

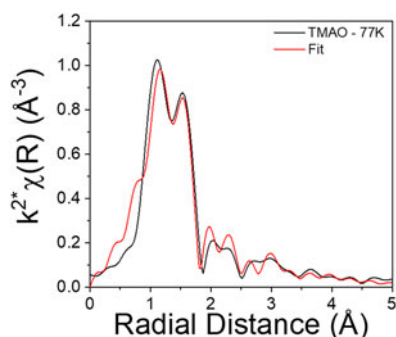


Figure 5. The experimental (black) and fitted (red) fit of the k-weight Fourier-transformed As K-edge EXAFS spectrum of TMAO dihydrate.

The As1–O2 and As1–C paths mostly describe the main peak in the EXAFS spectrum located at $\sim 0.8\text{--}2 \text{ \AA}$. The fitting result yields As1–O2 and As1–C distances of 1.65(1) and 1.87(1) \AA , respectively, in good agreement with distances obtained from the diffraction analysis. The third shell mostly describes minor features located at 2.5–4 \AA . Including the third shell scattering paths generally improves the quality of the fit, with R_{fit} decreasing from 0.033 to 0.019. This suggests that water molecules are present in the local structure and is generally in good agreement with the diffraction analysis. Both the As1–O7 and As1–O6 distances are slightly smaller than those obtained from the diffraction analysis, which may be a consequence of the O7–H20...O2 and O6–H17...O2 hydrogen bonds. The As1–O7 distance exhibits the greatest deviation, possibly because of the stronger O7–H20...O2 hydrogen bond drawing O7 atoms closer to the As1 atoms. Furthermore, the O7 atoms also exhibit a smaller σ^2 compared with the O6 atoms, suggesting that the O7 atoms experience less thermal and static disorder than the O6 atoms.

TABLE V. A summary of the As K-edge EXAFS fit results.

Global fitting parameters				
S_0^2	1.04(12)			
ΔE_0 (eV)	–1.9(0.6)			
R_{fit}	0.019			
Shell	Scatterer	CN	$R(\text{\AA})$	σ^2
1	O2	1	1.65(1)	0.002(1)
1	C	3	1.87(1)	0.003(2)
3	O7	1	3.52(4)	0.007(5)
3	O6	1	3.77(3)	0.034(10)

IV. DEPOSITED DATA

CIF and/or RAW data files were deposited with ICDD. You may request this data from ICDD at info@icdd.com.

ACKNOWLEDGEMENTS

The authors thank Andrey Rogachev for the use of the computing resources at the Illinois Institute of Technology. Additional thanks to Ning Chen and Weifeng Chen from beamline 06ID-1, and Burke Barlow, Erika Bergen, Toby Bond, Wajeeha Hassan, Danielle Veikle, and Jeff Warner from the CLS Industrial Science Group for assistance with the X-ray absorption spectroscopy data collection, which was part of a large arsenic speciation project. Two anonymous reviewers are also thanked for helpful suggestions which improved this manuscript. Research described in this paper was performed using beamlines 08B1-1 and 06ID-1 at the Canadian Light Source, which is supported by the Canadian Foundation for Innovation, the Natural Sciences and Engineering Research Council of Canada, the National Research Council Canada, the Canadian Institutes of Health

Research, the Government of Saskatchewan, Western Economic Diversification Canada, and the University of Saskatchewan.

- Agency for Toxic Substances and Disease Registry, ATSDR (2020). Priority list of hazardous substances. Available at: <http://www.atsdr.cdc.gov/SPL/index.html>.
- Boultif, A. and Louer, D. (2004). "Powder pattern indexing with the dichotomy method," *J. Appl. Crystallogr.* **37**, 724–731.
- Bruno, I. J., Cole, J. C., Kessler, M., Luo, J., Motherwell, W. D. S., Purkis, L. H., Smith, B. R., Taylor, R., Cooper, R. I., Harris, S. E., and Orpen, A. G. (2004). "Retrieval of crystallographically-derived molecular geometry information," *J. Chem. Inf. Comput. Sci.* **44**, 2133–2144.
- Bunker, G. (2010). *Introduction to XAFS: A Practical Guide to X-ray Absorption Fine Structure Spectroscopy* (Cambridge Press, New York).
- Capitani, E. M. D. (2011). "Arsenic toxicology – a review," in *Arsenic: Natural and Anthropogenic*, edited by F. Deschamps and J. Mutschallat (CRC Press, London), pp. 27–37.
- Chen, W. Q., Shi, Y. L., Wu, S. L., and Zhu, Y. G. (2016). "Anthropogenic arsenic cycles: a research framework and features," *J. Cleaner Production* **139**, 328–336.
- Cullen, W. R. and Reimer, K. J. (1989). "Arsenic speciation in the environment," *Chem. Rev.* **89**, 713–764.
- Cullen, W. R., Liu, Q., Lu, X., McKnight-Whitford, A., Peng, H., Popowich, A., Yan, X., Zhang, Q., Fricke, M., Sun, H., and Le, X. C. (2016). "Methylated and thiolated arsenic species for environmental and health research – a review on synthesis and characterization," *J. Environ. Sci.* **49**, 7–27.
- Dovesi, R., Orlando, R., Erba, A., Zicovich-Wilson, C. M., Civalieri, B., Casassa, S., Maschio, L., Ferrabone, M., De La Pierre, M., D'Arco, P., Noel, Y., Causa, M., Rerat, M., and Kirtman, B. (2014). "CRYSTAL14: a program for the *ab initio* investigation of crystalline solids," *Int. J. Quant. Chem.* **114**, 1287–1313.
- Favre-Nicolin, V., and Černý, R. (2002). "FOX, 'Free objects for crystallography': a modular approach to *ab initio* structure determination from powder diffraction," *J. Appl. Crystallogr.* **35**, 734–743.
- Fodje, M., Grochulski, P., Janzen, K., Labiuk, S., Gorin, J., and Berg, R. (2014). "08B1-1: an automated beamline for macromolecular crystallography experiments at the Canadian Light Source," *J. Synchrotron Rad.* **21**, 633–637.
- Foust, Jr., R. D., Bauer, A. M., Costanza-Robinson, M., Blinn, D. W., Prince, R. C., Pickering, I. J., and George, G. N. (2016). "Arsenic transfer and bio-transformation in a fully characterized freshwater food web," *Coord. Chem. Rev.* **306**, 558–565.
- Gatti, C., Saunders, V. R., and Roetti, C. (1994). "Crystal-field effects on the topological properties of the electron-density in molecular crystals – the case of urea," *J. Chem. Phys.* **101**, 10686–10696.
- George, G. R., Prince, R. C., Singh, S. P., and Pickering, I. J. (2009). "Arsenic K-edge X-ray absorption spectroscopy of arsenic in seafood," *Mol. Nutr. Food Res.* **53**, 552–557.
- Hanwell, M. D., Curtis, D. E., Lonie, D. C., Vandermeersch, T., Zurek, E., and Hutchison, G. R. (2012). "Avogadro: an advanced semantic chemical editor, visualization, and analysis platform," *J. Cheminform.* **4**, 17.
- Hunter, D. A., Goessler, W., and Francesconi, K. A. (1998). "Uptake of arsenate, trimethylarsine oxide, and arsenobetaine by the shrimp *Crangon crangon*," *Mar. Biol.* **131**, 543–552.
- Jiang, D. T., Chen, N., Zhang, L., Malgorzata, G., Wright, G., Igarashi, R., Beauregard, D., Kirkham, M., and McKibben, M. (2007). "XAFS at canadian light source," *AIP Conf. Proc.* **882**, 893–895.
- Koch, I., McPherson, K., Smith, P., Easton, L., Doe, K. G., and Reimer, K. J. (2007). "Arsenic bioaccessibility and speciation in clams and seaweed from a contaminated marine environment," *Mar. Pollut. Bull.* **54**, 586–594.
- Kresse, G. and Furthmüller, J. (1996). "Efficient iterative schemes for *ab initio* total-energy calculations using a plane-wave basis set," *Phys. Rev. B* **54**, 11169.
- Laugier, J. and Bochu, B. (2000). "LMGP-Suite Suite of Programs for the interpretation of X-ray Experiments," ENSP/Laboratoire des Matériaux et du Génie Physique, BP 46. 38042 Saint Martin d'Hères, France. Available at: <http://www.inpg.fr/LMGP> and <http://www.ccp14.ac.uk/tutorial/lmgp/>.
- Macrae, C. F., Bruno, I. J., Chisholm, J. A., Edgington, P. R., McCabe, P., Pidcock, E., Rodriguez-Monge, L., Taylor, R., van de Streek, J., and Wood, P. A. (2008). "Mercury CSD 2.0 – new features for the visualization and investigation of crystal structures," *J. Appl. Crystallogr.* **41**, 466–470.
- Materials Design (2016). *MedeA 2.20.4* (Materials Design Inc., Angel Fire, NM).
- Matschullat, J. (2011). "The global arsenic cycle revisited," in *Arsenic: Natural and Anthropogenic*, edited by F. Deschamps and J. Mutschallat (CRC Press, London), pp. 3–26.
- Momma, K. and Izumi, F. (2011). "VESTA 3 for three-dimensional visualization of crystal, volumetric and morphology data," *J. Appl. Crystallogr.* **44**, 1272–1276.
- Newville, M. (2004). *Fundamentals of XAFS* (University of Chicago, Chicago), 1.7 ed.
- Ng, Y. S., Rodley, G. A., and Robinson, W. T. (1977). "Tri- μ -(trimethylarsine oxide)-hexakis(trimethylarsine oxide)dicalcium(II) tetra-perchlorate – a dinuclear calcium complex," *Acta Crystallogr. B* **33**, 931–934.
- O'Boyle, N., Banck, M., James, C. A., Morley, C., Vandermeersch, T., and Hutchison, G. R. (2011). "Open Babel: an open chemical toolbox," *J. Cheminform.* **3**, 33.
- Peintinger, M. F., Vilela Oliveira, D., and Bredow, T. (2013). "Consistent Gaussian basis sets of triple-zeta valence with polarization quality for solid-state calculations," *J. Comput. Chem.* **34**, 451–459.
- Pickett, A. W., McBride, B. C., and Cullen, W. C. (1988). "Metabolism of trimethylarsine," *Appl. Organomet. Chem.* **2**, 479–482.
- Rammohan, A. and Kaduk, J. A. (2018). "Crystal structures of alkali metal (Group 1) citrate salts," *Acta Crystallogr. B* **74**, 239–252.
- Ravel, B. and Newville, M. (2005). "ATHENA, ARTEMIS, HEPHAESTUS: data analysis for X-ray absorption spectroscopy using IFFEFIT," *J. Synchrotron Rad.* **12**, 537–541.
- Rehy, L. and Albers, R. (1990). "Scattering-matrix formulation of curved-wave multiple-scattering theory: application to X-ray-absorption fine structure," *Phys. Rev. B* **41**, 8139–8149.
- Savage, L., Carey, M., Hossain, M., Rafiqul Islam, M., Mangala, P., de Silva, C. S., Williams, P. N., and Meharg, A. A. (2017). "Elevated trimethylarsine oxide and inorganic arsenic in northern hemisphere summer monsoonal wet deposition," *Environ. Sci. Technol.* **51**, 12210–12218.
- Smith, P. G., Koch, I., Gordon, R. A., Mandoli, D. F., Chapman, B. D., and Reimer, K. J. (2005). "X-ray absorption near-edge structure analysis of arsenic species for application to biological environmental samples," *Environ. Sci. Technol.* **39**, 248–254.
- Thompson, P., Cox, D. E., and Hastings, J. B. (1987). "Rietveld refinement of Debye-Scherrer synchrotron X-ray data from Al_2O_3 ," *J. Appl. Crystallogr.* **20**, 79–83.
- Toby, B. H. and Von Dreele, R. B. (2013). "GSAS II: the genesis of a modern open-source all-purpose crystallography software package," *J. Appl. Crystallogr.* **46**, 544–549.
- Van de Streek, J. and Neumann, M. A. (2014). "Validation of molecular crystal structures from powder diffraction data with dispersion corrected density functional theory (DFT-D)," *Acta Crystallogr. B* **70**, 1020–1032.